Journal of Power Sources 196 (2011) 10692–10697

Contents lists available at SciVerse ScienceDirect

Journal of Power Sources

journal homepage: www.elsevier.com/locate/jpowsour

Improved rate capability of carbon coated $Li_{3.9}Sn_{0.1}Ti_5O_{12}$ porous electrodes for Li-ion batteries

Biao Zhang, Zhen-Dong Huang, Sei Woon Oh, Jang-Kyo Kim*

Department of Mechanical Engineering, Hong Kong University of Science and Technology, Clear Water Bay, Hong Kong, China

ARTICLE INFO

Article history:
Received 1 June 2011
Received in revised form 20 July 2011
Accepted 6 August 2011
Available online 7 September 2011

Keywords:
Lithium titanate
Doping
Anode
Li-ion batteries

ABSTRACT

A new sol–gel process is developed to modify the $Li_4Ti_5O_{12}$ anode material for improved rate capability. The new process brings about the following effects, namely (i) doping of Sn^{2+} to form $Li_{3.9}Sn_{0.1}Ti_5O_{12}$, (ii) carbon coating and (iii) creation of a porous structure. The doping of Sn^{2+} results in the lattice distortion without changing the phase composition. A thin layer of amorphous carbon is coated on the doped particles that contain numerous nanopores. The rate capability of the anode material made from the modified powder is significantly improved when discharged at high current rates due to the reduced charge transfer resistance.

1. Introduction

While Li-ion batteries (LIBs) have gained great success for application in portable electronics, they require improvements in various electrochemical properties, including cyclic life, power and energy densities and safety, to be able to become the most promising power source in future electric vehicles. In particular, graphite – the current anode material – has slow Li^+ diffusion, limiting the power density of LIBs. The low charge/discharge plateau of graphite may lead to the deposition of metallic Li on the electrode at high current densities, causing serious safety problems [1]. $Li_4Ti_5O_{12}$ is known to be one of the best substitutes for the graphite anode in LIBs. It undergoes a phase transformation between spinel $Li_4Ti_5O_{12}$ and rock-salt $Li_7Ti_5O_{12}$ during the Li^+ intercalation/extraction process, and displays a discharge plateau at about 1.5 V (vs. Li/Li^+) and a theoretical capacity of 175 mAh g^{-1}. The $Li_4Ti_5O_{12}$ anode possess several advantages: (i) the high charge/discharge plateau avoids the safety problem caused by the deposition of metallic Li; and (ii) the low volumetric change occurring during the phase transformation, i.e. less than 1%, can give rise to excellent cyclic performance [2]. The $Li_4Ti_5O_{12}$ anode was coupled with cathode materials made from $LiFePO_4/LiNi_{0.5}Mn_{1.5}O_4$ at an operating voltage of 1.8 V/3 V. These systems showed excellent electrochemical properties and demonstrated potential applications in electric vehicles [3,4].

Nevertheless, a main obstacle that impedes the widespread applications of $Li_4Ti_5O_{12}$ is its poor conductivity with associated poor charge/discharge properties at high current rates. Several approaches have been adopted to improve the rate capability of $Li_4Ti_5O_{12}$, including: (i) doping with ions, such as Br^-, Li^+, Mg^{2+}, Zn^{2+}, Ni^{2+}, Cr^{3+}, Al^{3+}, La^{3+}, V^{5+}, Nb^{5+} and Ta^{5+} at Li, Ti or O sites to improve the electronic conductivity [5–15]; (ii) coating with a conductive phase, such as amorphous carbon, carbon nanotube or Ag [16–19], where the second phase forms a conductive channel for fast transfer of Li^+ and electrons; and (iii) fabrication of a porous structure that can absorb the electrolyte and shorten the solid state diffusion length of Li^+ [20]. Sn-based anodes possess extremely high capacities compared to graphite and $Li_4Ti_5O_{12}$ anodes. SnO_x has been incorporated into a $Li_4Ti_5O_{12}$ matrix to increase the capacity of $Li_4Ti_5O_{12}$, where $Li_4Ti_5O_{12}$ acts as a buffer layer to alleviate the volume change of SnO_x during charge/discharge [21,22]. A thermal treatment is required to increase the crystallinity of SnO_x, while it may also introduce Sn^{2+} into the lattice of $Li_4Ti_5O_{12}$. However, the effects of Sn^{2+} doping are not fully understood, necessitating further studies.

The review of the above studies intuitively hints that substantial synergy can be achieved when the ameliorating effects, such as doping, carbon coating and porous structure, are combined together. The improved capacities reported in the previous studies are usually based on single effect as a result of an individual modification process. In this study, one-step sol–gel process is developed to dope $Li_4Ti_5O_{12}$ with Sn^{2+} to improve the conductivity, while a carbon coating and porous structure are simultaneously created in the $Li_4Ti_5O_{12}$ powder.

* Corresponding author. Tel.: +852 2358 7207; fax: +852 2358 1543.
E-mail address: mejkkim@ust.hk (J.-K. Kim).

0378-7753/$ – see front matter © 2011 Elsevier B.V. All rights reserved.
doi:10.1016/j.jpowsour.2011.08.114

2. Experimental

$Li_4Ti_5O_{12}$ was synthesized based on a sol–gel method [23]. Titanium *iso*-propoxide and lithium acetate dihydrate were mixed in 50 mL of ethanol. Excessive Li (10 mol%) was added to compensate the evaporation during synthesis at a high temperature. After stirring for 10 min, the color of the solution changed from yellow to white. Stirring was continued at 80 °C until gel was formed, which was dried at 60 °C for 24 h in an oven. The dry product was ground to fine powder, and was then calcinated at 800 °C for 12 h in a N_2 atmosphere to obtain $Li_4Ti_5O_{12}$ powder. The procedure used for the preparation of Sn^{2+} doped $Li_4Ti_5O_{12}$ powder was generally similar to that of undoped powder, except the addition of $SnCl_2\ 2H_2O$ to the solution according to the formula of $Li_{3.9}Sn_{0.1}Ti_5O_{12}$. During the whole process, the color of the solution remained light yellow.

The phase structures of the powders were determined on an X-ray diffraction (XRD) system (PW1830, Philips) with Cu Kα radiation from 10° to 70°. Thermogravimetric analysis 178 (TGA) were conducted on a TGA/DTA 92 Setaram II testing system in air at a heating rate of 5 °C min^{-1}. X-ray photoelectron spectroscopy (XPS, PHI5600, Physical Electronics) was employed to evaluate the chemical states of the powders using a monochromatic Al Kα X-ray as the excitation source at an electron voltage of 14 kV. The C 1s peak at 285.0 eV was used as the binding energy reference. Quantitative structural analysis of powders was conducted on a RM3000 Micro Raman System (Renishaw PLC) with argon laser excitation of 514 nm. Field emission transmission electron microscope (FETEM, JEOL 2010F) and scanning electron microscope (SEM, JEOL 6700F) were used to characterize the morphologies. The specific surface area was measured using the Brunauer–Emmett–Teller (BET) method on a Coulter SA 3100 Surface Area instrument. The sample powders were pressed into circular pellets of 12.5 mm in diameter and about 1 mm in thickness, and were subsequently sintered at 800 °C for 12 h in a N_2 atmosphere. Silver paste was applied on the top and bottom surfaces of the sample and the programmable curve tracer (370A) machine was employed to measure the conductivity.

The electrochemical tests were carried out using CR2032 coin cells. The sample slurry was prepared by mixing the active materials and carbon black with polyvinylidene fluoride (PVDF) binder in a weight ratio of 80:10:10 after magnetic stirring in N-methy1-2-pyrrolidone for 4 h. The slurry was coated onto the copper foil from which pellets of 12 mm in diameter were cut as electrodes. The cells were assembled in an Ar-filled glove box with a lithium foil as the counter electrode, 1 M $LiPF_6$ in ethyl carbonate (EC)/dimethyl carbonate (DMC) (1:1 by volume) as electrolyte and a microporous polyethylene film (Celgard 2400) as separator. The coin cells were cycled at different current densities between 1 and 3 V on a LAND 2001 CT battery tester. The charge and discharge current densities were maintained identical during each cycle. The electrochemical impedance spectroscopy (EIS) was carried out in the frequency range from 100 kHz to 10 mHz on a CHI660 electrochemical workstation. Two $Li_{3.9}Sn_{0.1}Ti_5O_{12}$/Li cells were discharged to 1 V and charged to 3 V in the first cycle. After the charge/discharge cycles, these cells were disassembled and washed with DMC, and laid to dry in the glove box. The dried electrodes were used for XRD characterization.

3. Results and discussion

Fig. 1(a) shows the XRD patterns of $Li_4Ti_5O_{12}$ and $Li_{3.9}Sn_{0.1}Ti_5O_{12}$ powders. All major peaks were in accordance with the standard diffraction peaks of $Li_4Ti_5O_{12}$ with PDF number of 72-0426. The small peaks at about 27.5° and 44.6° are attributed to hexagonal TiO phase (PDF number: 85-2084) due

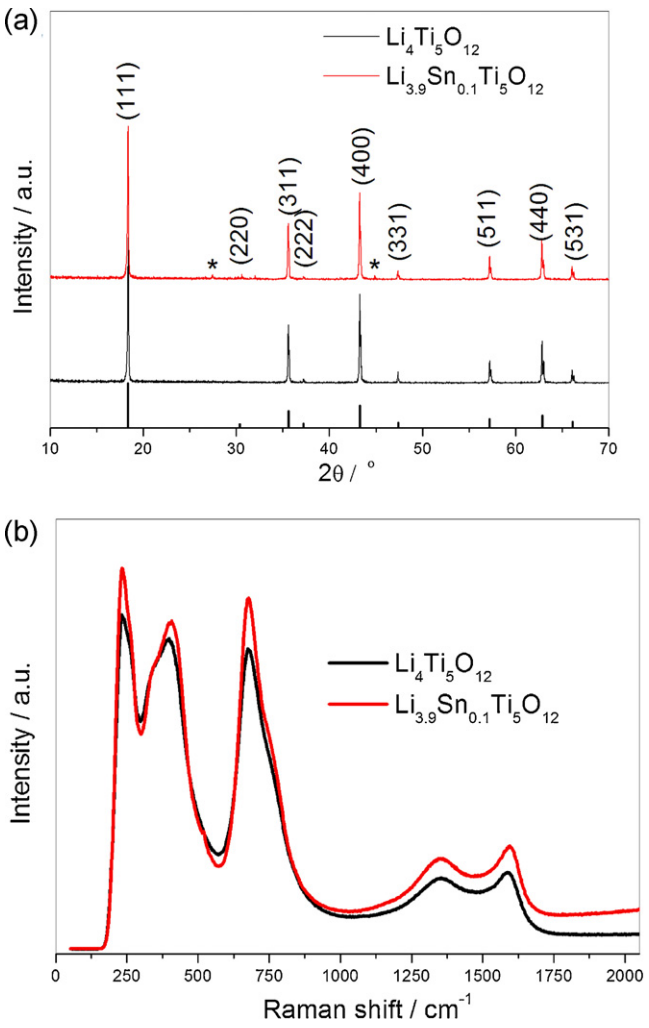

Fig. 1. (a) XRD patterns and (b) Raman spectra of $Li_4Ti_5O_{12}$ and $Li_{3.9}Sn_{0.1}Ti_5O_{12}$ powders.

to the evaporation of Li during the synthesis process. The unit cell parameters calculated using the Bragg's law were 8.3573 and 8.3611 Å for $Li_4Ti_5O_{12}$ and $Li_{3.9}Sn_{0.1}Ti_5O_{12}$, respectively. They were calculated based on a least square method with an estimated error of 4×10^{-4} Å. The increased lattice parameter is ascribed to the larger Sn^{2+} (1.02 Å) that occupied the sites of the smaller Li^+ (0.68 Å) [24], confirming the entrance of Sn^{2+} into the crystal lattice. The (2 2 0) peak is attributed to the scattering power of Li^+ located at the tetrahedral (8a) site in $Li_4Ti_5O_{12}$. Sn^{2+} has an inherently higher scattering power than Li^+. The relative intensity ratio, $I_{(220)}/I_{(111)}$, increased from 0.018 to 0.038 after doping with Sn^{2+} which replaced Li^+ [7].

The Raman spectra shown in Fig. 1(b) indicate five vibration peaks at about 237, 264, 344, 400, 675 cm^{-1}, which are consistent with the spinel structure of $Li_4Ti_5O_{12}$ (A1g + Eg + 3F2g). The frequency in the range of Raman shift 400–550 cm^{-1} are assigned to Li–O stretches in "LiO_4" tetrahedron [25,26]. The Raman bands corresponding to the Li–O vibration had a red shift from 400 to 408 cm^{-1} after doping due to the substitution of Sn^{2+} for Li^+, which enhanced the cation-oxygen bonding [13]. The two peaks at 1355 and 1587 cm^{-1} correspond to D and G bands of carbon, respectively.

The XPS was used to evaluate the surface chemistry of the powders and thus to clarify the valance states of Ti and Sn ions. The general spectra given in Fig. 2(a) identified strong signals of C, O and Ti in $Li_4Ti_5O_{12}$, and Sn in addition to the three elements in

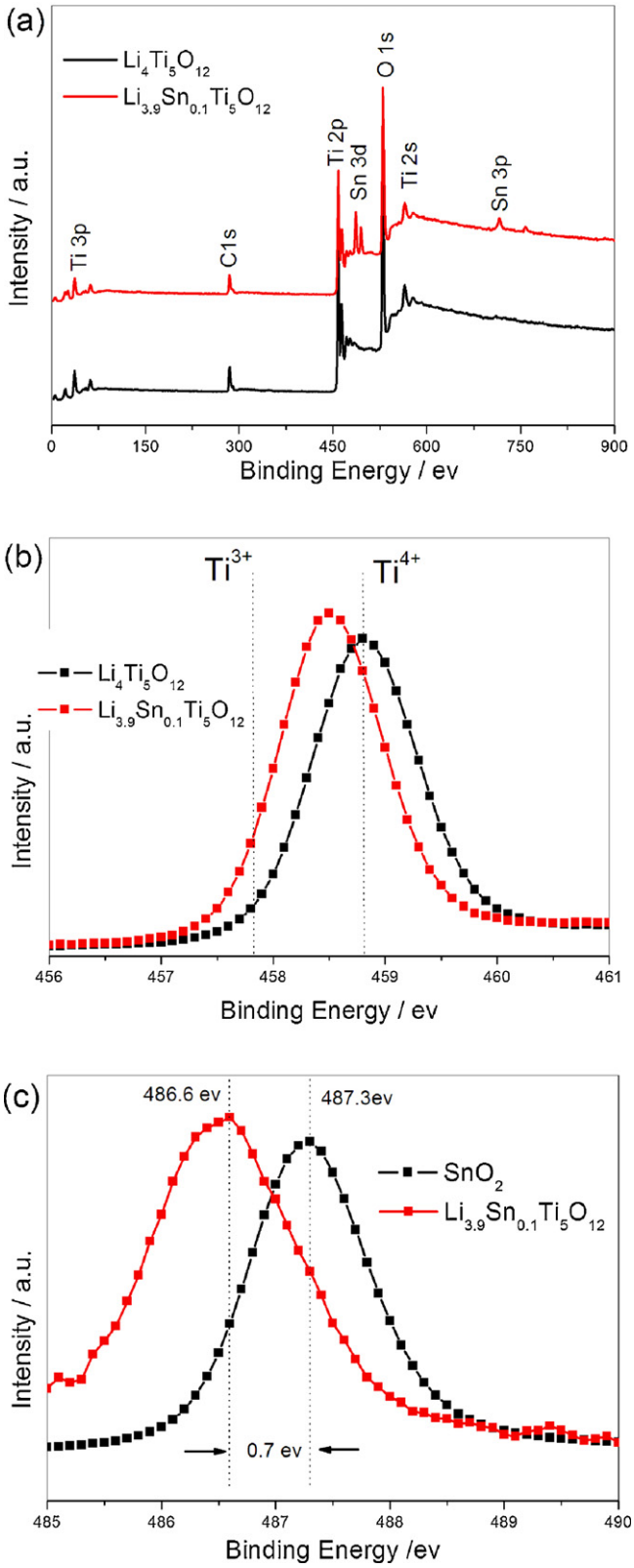

Fig. 2. (a) XPS general spectra, (b) Ti $2p_{3/2}$ and (c) Sn $3d_{5/2}$ specific spectra of $Li_4Ti_5O_{12}$ and $Li_{3.9}Sn_{0.1}Ti_5O_{12}$ powders.

$Li_{3.9}Sn_{0.1}Ti_5O_{12}$. A weak signal at 54.4 eV corresponding to Li 1s was also observed. The peaks at 285.0 eV are ascribed to the amorphous carbon coated on the surface of the particles, which are in agreement with the Raman results. The two peaks of Sn 3d, i.e. Sn $3d_{5/2}$ and Sn $3d_{3/2}$, were identified at 486.6 eV and 495.1 eV,

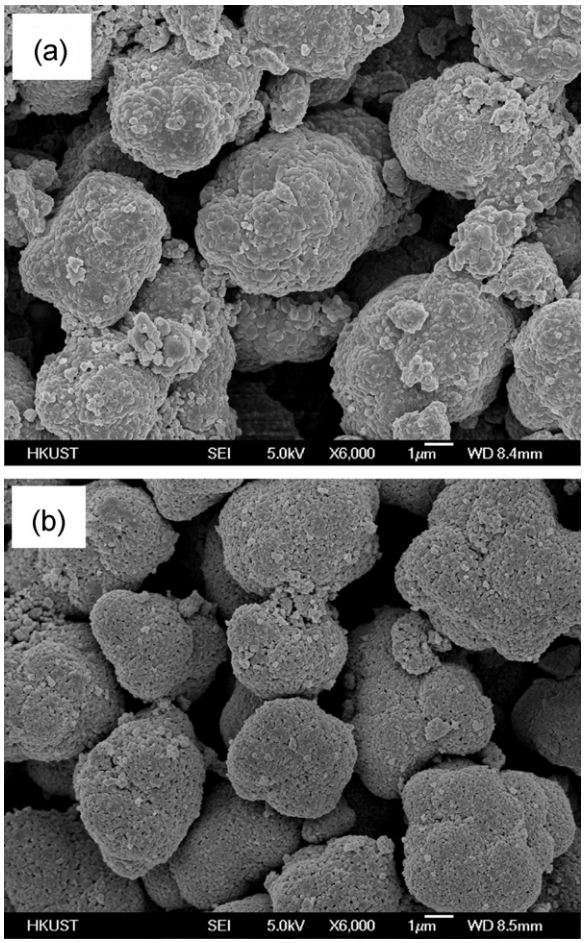

Fig. 3. (a) Surface morphologies of (a) $Li_4Ti_5O_{12}$ (b) $Li_{3.9}Sn_{0.1}Ti_5O_{12}$ powders.

respectively, which reflect the presence of Sn element in $Li_{3.9}Sn_{0.1}Ti_5O_{12}$. The binding energy for Ti $2p_{3/2}$ presented a shift of 0.3 eV to the position of Ti^{3+} (457.8 eV [27]) after doping (Fig. 2(b)), suggesting a mixed Ti^{4+}/Ti^{3+} valence of Ti ions [28]. The binding energy for Sn $3d_{5/2}$ was used to study the valence of Sn ions in

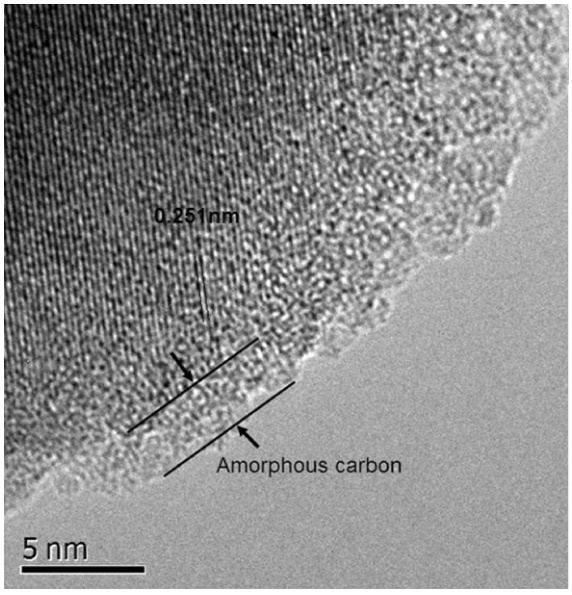

Fig. 4. TEM micrograph of $Li_{3.9}Sn_{0.1}Ti_5O_{12}$ powder.

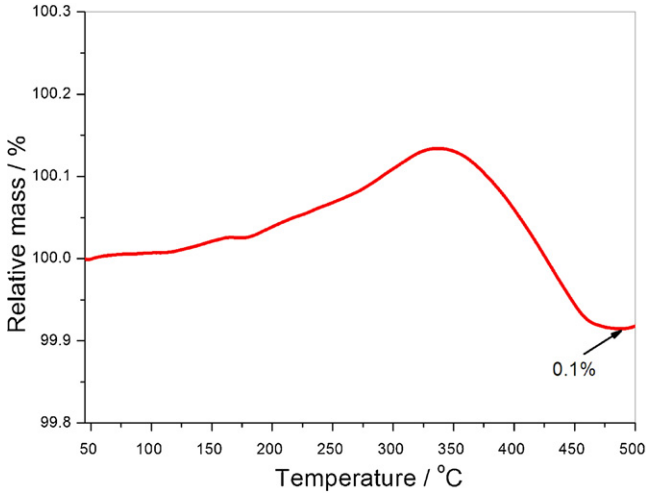

Fig. 5. TGA curve of $Li_{3.9}Sn_{0.1}Ti_5O_{12}$.

$Li_{3.9}Sn_{0.1}Ti_5O_{12}$ based on SnO_2 as a reference (Fig. 2(c)). There was a binding energy difference of 0.7 eV between the Sn $3d_{5/2}$ peaks of SnO_2 and $Li_{3.9}Sn_{0.1}Ti_5O_{12}$, in agreement with the chemical shift between Sn^{4+} and Sn^{2+} reported previously [29]. These observations indicate that Sn ions are in the state of Sn^{2+} in $Li_{3.9}Sn_{0.1}Ti_5O_{12}$.

The SEM images presented in Fig. 3 indicate that both powders before and after doping maintained a similar spherical shape. These primary particles had a diameter ranging from several to 10 μm, and consisted of numerous secondary nanoparticles of a few hundred nanometers in diameter. Nanopores were found on the surface of the doped $Li_{3.9}Sn_{0.1}Ti_5O_{12}$ primary particles whereas pores were absent on the $Li_4Ti_5O_{12}$ particles. In view of the fact that the $Li_{3.9}Sn_{0.1}Ti_5O_{12}$ gel had a yellow color while the $Li_4Ti_5O_{12}$ gel was white, titanium *iso*-propoxide was not fully hydrolyzed due to the addition of $SnCl_2$ $2H_2O$ during the synthesis of $Li_{3.9}Sn_{0.1}Ti_5O_{12}$. Upon calcination, titanium *iso*-propoxide was decomposed to TiO_2, generating H_2O and CO_2 gas. After reaction with lithium source, the $Li_{3.9}Sn_{0.1}Ti_5O_{12}$ nanoparticles tended to aggregate to form primary spherical particles of several micrometers in diameter. When the evaporation of the gas generated by the decomposition of titanium *iso*-propoxide occurred, nanopores were naturally created between the secondary nanoparticle. The presence of nanopores was further evidenced by the substantial increase in the BET surface area from 3.4 $m^2\ g^{-1}$ to 6.9 $m^2\ g^{-1}$ after Sn^{2+} doping.

The TEM micrograph of $Li_{3.9}Sn_{0.1}Ti_5O_{12}$ shown in Fig. 4 indicates that the distance between the crystal lines was 0.251 nm, corresponding to the (3 1 1) face. A thin layer of amorphous carbon was present on the particle surface, which is attributed to carbonization of the organic precursor during calcination in an inert atmosphere. This observation is in agreement with the Raman and XPS results. Titanium *iso*-propoxide was hydrolyzed during the production of $Li_4Ti_5O_{12}$. The amorphous carbon was initially formed on the surface of Li_2O due to carbonization of acetate in lithium acetate, and later coated on $Li_4Ti_5O_{12}$ and $Li_{3.9}Sn_{0.1}Ti_5O_{12}$ following the reaction

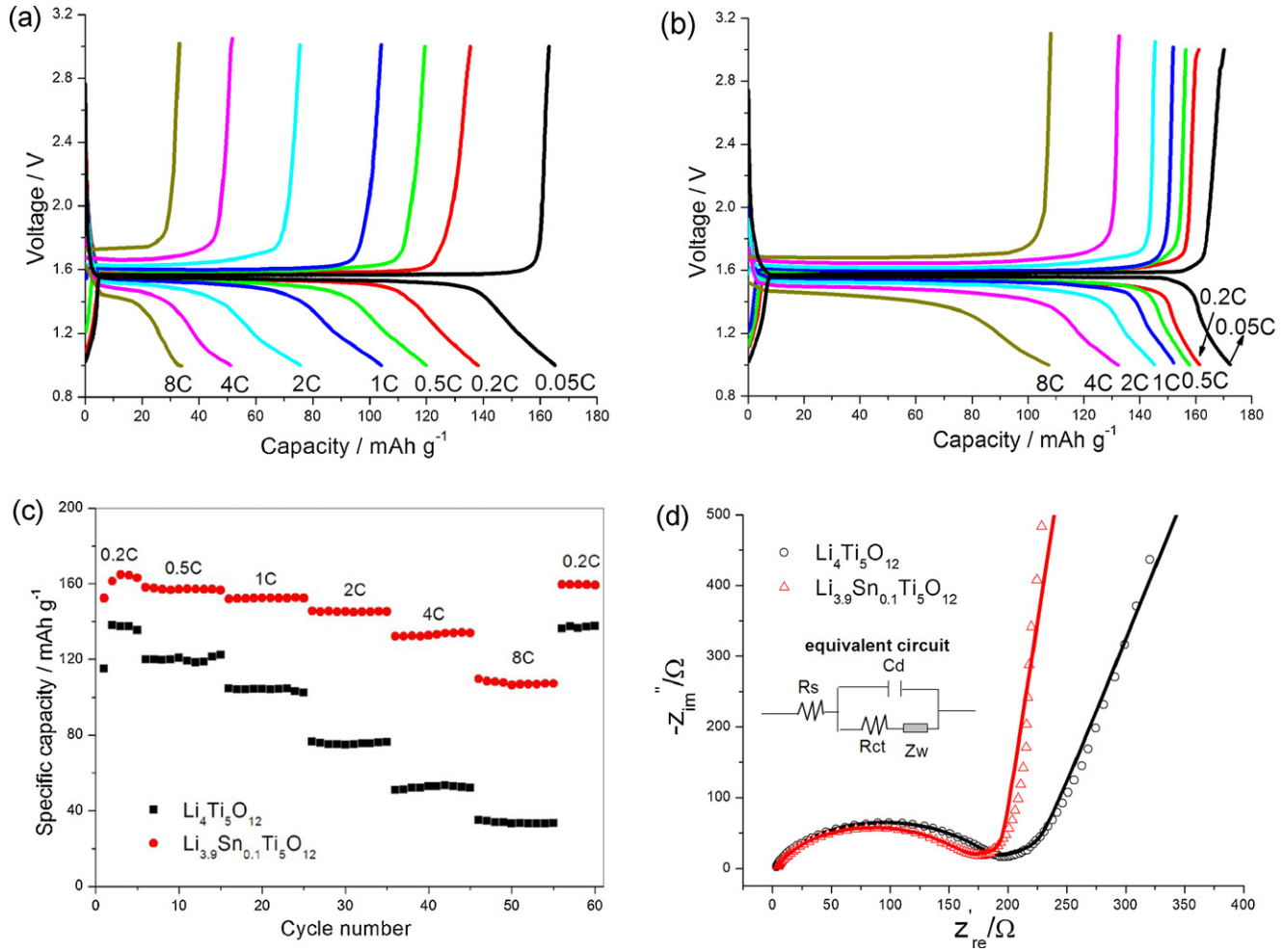

Fig. 6. Charge/discharge curves of (a) $Li_4Ti_5O_{12}$ and (b) $Li_{3.9}Sn_{0.1}Ti_5O_{12}$ cells; (c) cyclic performance at different currents; and (d) EIS spectra: hollow points represent experimental data and solid lines represent data fitted by Zview 2.0 software.

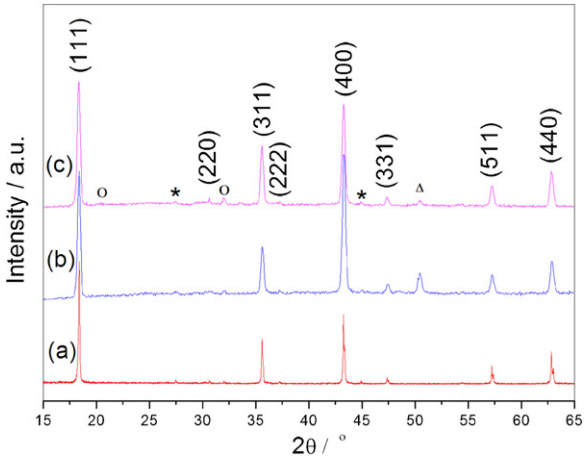

Fig. 7. Ex situ XRD patterns of $Li_{3.9}Sn_{0.1}Ti_5O_{12}$ during the first cycle at different charge/discharge voltage: (a) pristine; (b) after discharging to 1 V; (c) after charging to 3 V. The peaks marked with asterisks (*), circles (○) and triangles (△) correspond to the diffractions of TiO, PVDF and copper, respectively.

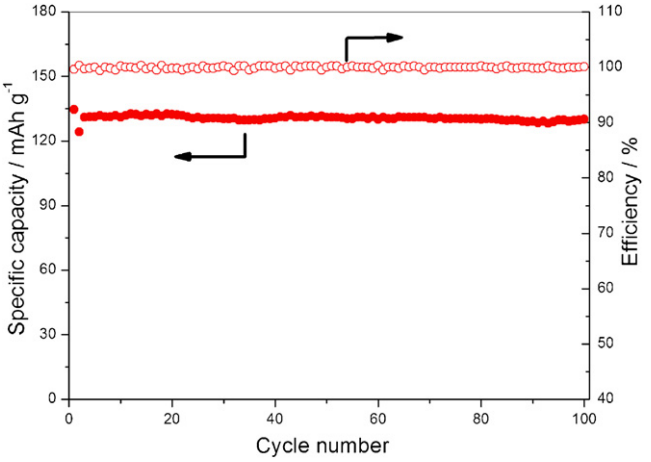

Fig. 8. Cyclic performance of $Li_{3.9}Sn_{0.1}Ti_5O_{12}$ cells discharged at 5 C and the corresponding efficiency.

with TiO_2. The amount of carbon in $Li_{3.9}Sn_{0.1}Ti_5O_{12}$ was characterized by TGA, as shown in Fig. 5. Sn^{2+} and Ti^{3+} were oxidized to Sn^{4+} and Ti^{4+} due to the high temperature treatment in air, resulting in the formation of $Li_{3.9}Sn_{0.1}Ti_5O_{12.15}$. According to the formula, an increase of 0.5 wt.% was expected, but a small reduction of 0.1 wt.% was recorded at 500 °C, indicating the presence of 0.6 wt.% carbon in the sample.

The capacities of the electrodes prepared from $Li_4Ti_5O_{12}$ and $Li_{3.9}Sn_{0.1}Ti_5O_{12}$ powders were measured at different current rates, as shown in Fig. 6. The capacity of $Li_{3.9}Sn_{0.1}Ti_5O_{12}$ discharged at 0.05 C was 172 mAh g^{-1}, which was higher than the corresponding value of 165 mAh g^{-1} for $Li_4Ti_5O_{12}$. As the discharge current rate increased, the capacities gradually decreased. After cycling at different current rates for 50 cycles, the capacities of both electrodes were restored to their original values when the discharge current was reduced to 0.2 C. Fig. 6(c) clearly indicates excellent cyclic performance of both materials, with the doped $Li_{3.9}Sn_{0.1}Ti_5O_{12}$ powder having much better rate capability than the neat $Li_4Ti_5O_{12}$ powder. The EIS spectra and impedance data analyzed on the basis of the equivalent circuit are shown in Fig. 6(d). The charge transfer resistance (R_{ct}) represents the kinetic resistance of charge transfer at the electrode/electrolyte boundary or intrinsic charge transfer resistance of the electrodes. R_{ct} was 160 Ω for the $Li_{3.9}Sn_{0.1}Ti_5O_{12}$ electrode, which is lower than 181 Ω for the $Li_4Ti_5O_{12}$ electrode, confirming the reduced charge transfer resistance after doping. The reduction in R_{ct} is attributed partly to the improved electronic conductivity after Sn^{2+} doping: $Li_{3.9}Sn_{0.1}Ti_5O_{12}$ had a conductivity of 9.1×10^{-8} S cm^{-1}, which is almost six times higher than 1.6×10^{-8} S cm^{-1} for $Li_4Ti_5O_{12}$.

The improvement in conductivity is the outcome of the substitution of Li^+ by Sn^{2+}. It follows that the difference in charge should be compensated by a reduction in the equivalent number of Ti cations from Ti^{4+} to Ti^{3+} [7,15]. The improved conductivity by doping gave rise to an increased rate capability when discharged at high current rates. The porous structure was also beneficial to the discharge properties at high current rates because of the increased intercalating sites for Li^+. The electrolyte could be absorbed into the nanopores, which in turn shortened the solid state transfer length, facilitating faster transfer of Li^+.

To identify if there were any additional structural changes during Li^+ insertion and extraction, the crystalline structure of the $Li_{3.9}Sn_{0.1}Ti_5O_{12}$ electrode was characterized after discharging to 1 V followed by charging to 3 V, as shown in Fig. 7. Some extra peaks related to PVDF (binder) and copper (current collector) were found. The relative intensity ratio, $I_{(400)}/I_{(111)}$, increased from 0.57 to 1.12 after discharging to 1 V because of the increased amount of Li^+ at the octahedral (16c) sites [30]. No evidence of the formation of a new crystalline phase was detected and the distortion of the pristine lattice was negligible. This result suggested that Sn^{2+} doping did not affect the structural changes during Li^+ insertion and extraction.

To evaluate the cyclic performance of carbon coated $Li_{3.9}Sn_{0.1}Ti_5O_{12}$ at a high current rate, the anode cell was subject to charge/discharge at 5 C for 100 cycles, and the results are shown in Fig. 8. The capacity of the $Li_{3.9}Sn_{0.1}Ti_5O_{12}$ cell maintained at 130 mAh g^{-1} with excellent capacity retention. Table 1 compares the result of the current study with the rate capabilities taken from the literature for various ion-doped $Li_4Ti_5O_{12}$ electrodes discharged to 1 V. The performance of $Li_{3.9}Sn_{0.1}Ti_5O_{12}$/C obtained in this study is considered highly comparable or even much better than the majority of $Li_4Ti_5O_{12}$ anodes.

Table 1
Comparison of rate performances for various ion-doped $Li_4Ti_5O_{12}$.

Samples	Synthesis method	Discharge current	Capacity (mAh g^{-1})	Reference
$Li_{3.9}Sn_{0.1}Ti_5O_{12}$/C	Sol–gel	5 C	130	Current study
$Li_4Ti_5O_{11.8}Br_{0.2}$	Solid-state	10 C	100	[5]
$Li_{4.1}Ti_{4.9}O_{12}$	Solid-state	4 C	139	[6]
$Li_{3.75}Mg_{0.25}Ti_5O_{12}$	Solid-state	2 mA cm^{-2}	90	[7]
$Li_{3.5}Zn_{0.5}Ti_5O_{12}$	Solid-state	4 C	108	[8]
$Li(Ni_{1/6}Li_{2/9}Ti_{1/9})Ti_{3/2}O_4$	Solid-state	5 C	100	[9]
$Li[CrTi]O_4$	Sol–gel	2 C	88	[10]
$Li_{3.9}Al_{0.1}Ti_5O_{12}$	Solid-state	3 C	120	[11]
La^{3+} doped $Li_4Ti_5O_{12}$/C	Sol–gel	2 C	136	[12]

4. Conclusion

A sol–gel approach is developed to synthesize $Li_{3.9}Sn_{0.1}Ti_5O_{12}$ anode material by doping $Li_4Ti_5O_{12}$ particles with Sn^{2+}. The process leads to two major changes in the structure: (i) coating of a thin amorphous carbon layer on the surface; and (ii) creation of numerous nanopores. These changes have ameliorating effects on electrochemical properties of anode cells made from $Li_{3.9}Sn_{0.1}Ti_5O_{12}$ powder: the specific capacities of the doped $Li_{3.9}Sn_{0.1}Ti_5O_{12}$ are much higher than the corresponding values of neat $Li_4Ti_5O_{12}$ when discharged at both low and high current densities. They also present almost 100% capacity retention after 100 cycles of charge/discharge at 5 C. Synergy of several enhancing mechanisms is responsible for the improved electrochemical properties of carbon coated $Li_{3.9}Sn_{0.1}Ti_5O_{12}$ porous electrodes.

Acknowledgements

This project was supported by the Research Grants Council (Project code: 614010, 613811) and the Innovation and Technology Fund (Project code: GHP/028/08SZ) of Hong Kong SAR. The authors also appreciate the technical assistance from the Materials Characterization and Preparation Facilities (MCPF) of HKUST. BZ, ZDH and SWO are supported partly by the Postgraduate Scholarship through the Nanoscience and Technology Program of the School of Engineering, HKUST.

References

[1] K.D. Shyamal, A.J. Bhattacharyya, J. Phys. Chem. C 113 (2009) 17367–17371.
[2] T. Ohzuku, A. Ueda, N. Yamamoto, J. Electrochem. Soc. 142 (1995) 1431–1435.
[3] X. Hu, Y. Huai, Z. Lin, J. Suo, Z. Deng, J. Electrochem. Soc. 154 (2007) A1026–A1030.
[4] H.F. Xiang, X. Zhang, Q.Y. Jin, C.P. Zhang, C.H. Chen, X.W. Ge, J. Power Sources 183 (2008) 355–360.
[5] Y.L. Qi, Y.D. Huang, D.Z. Jia, S.J. Bao, Z.P. Guo, Electrochim. Acta 54 (2009) 4772–4776.
[6] H. Ge, N. Li, D.Y. Li, C.S. Dai, D.L. Wang, Electrochem. Commun. 10 (2008) 1031–1034.
[7] C.H. Chen, J.T. Vaughey, A.N. Jansen, D.W. Dees, A.J. Kahaian, T. Goacher, M.M. Thackeray, J. Electrochem. Soc. 148 (2001) A102–A104.
[8] B. Zhang, H.D. Du, B.H. Li, F.Y. Kang, Electrochem. Solid State Lett. 13A (2010) 36–38.
[9] J. Kim, S.W. Kim, H. Gwon, W.S. Yoon, K. Kang, Electrochim. Acta 54 (2009) 5914–5918.
[10] Y.K. Sun, D.J. Jung, Y.S. Lee, K.S. Nahm, J. Power Sources 125 (2004) 242–245.
[11] H.L. Zhao, Y. Li, Z.M. Zhu, J. Lin, Z.H. Tian, R.L. Wang, Electrochim. Acta 53 (2008) 7079–7083.
[12] J. Gao, C. Jiang, C. Wan, J. Electrochem. Soc. 157 (2010) K39–K42.
[13] T.F. Yi, J. Shu, Y.R. Zhu, X.D. Zhu, R.S. Zhu, A.N. Zhou, J. Power Sources 195 (2010) 285–288.
[14] T.F. Yi, Y. Xie, J. Shu, Z. Wang, C.B. Yue, R.S. Zhu, H.B. Qiao, J. Electrochem. Soc. 158 (2011) A266–A274.
[15] J. Wolfenstine, J.L. Allen, J. Power Sources 180 (2008) 582–585.
[16] G.J. Wang, J. Gao, L.J. Fu, N.H. Zhao, Y.P. Wu, T. Takamura, J. Power Sources 174 (2007) 1109–1112.
[17] J.J. Huang, Z.Y. Jiang, Electrochim. Acta 53 (2008) 7756–7759.
[18] S.H. Huang, Z.Y. Wen, X.J. Zhu, Z.H. Gu, Electrochem. Commun. 6 (2004) 1093–1097.
[19] L.F. Shen, C.Z. Yuan, H.J. Luo, X.G. Zhang, K. Xu, F. Zhang, J. Mater. Chem. 21 (2011) 761–767.
[20] E.M. Sorensen, S.J. Barry, H.K. Jung, J.R. Rodinelli, J.T. Vaughey, K.R. Poeppelmeier, Chem. Mater. 18 (2006) 482–489.
[21] R. Cai, X. Yu, X.Q. Liu, Z.P. Shao, J. Power Sources 195 (2010) 8244–8250.
[22] Y.Y. Wang, Y.J. Hao, Q.Y. Lai, J.Z. Lu, Y.D. Chen, X.Y. Ji, Ionics 14 (2008) 85–88.
[23] M. Venkateswarlu, C.H. Chen, J.S. Do, C.W. Lin, T.C. Chou, B.J. Hwang, J. Power Sources 146 (2005) 204–208.
[24] J.A. Dean, Langes Chemistry Handbook, 13th ed., Science Press, Beijing, 1991.
[25] D.Z. Liu, W. Hayes, M. Kurmoo, M. Dalton, C. Chen, Physica C 235–240 (1994) 1203–1204.
[26] L. Aldon, P. Kubiak, M. Womes, J.C. Jumas, J.O. Fourcade, J.L. Tirado, J.I. Corredor, C.P. Vicente, Chem. Mater. 16 (2004) 5721–5725.
[27] F. Werfel, O. Brummer, Phys. Scr. 28 (1983) 92–96.
[28] Y.K. Sun, S.T. Myung, B.C. Park, J. Prakash, I. Belharouak, K. Amine, Nat. Mater. 8 (2009) 320–324.
[29] J.M. Themlin, M. Chtaib, L. Henrard, P. Lambin, J. Darville, J.M. Gilles, Phys. Rev. B 46 (1992) 2460–2466.
[30] H. Ge, N. Li, D.Y. Li, C.S. Dai, D.L. Wang, J. Phys. Chem. C 113 (2009) 6324–6326.